J. Fluid Mech. (2016), *vol.* 800, R2, doi:10.1017/jfm.2016.433

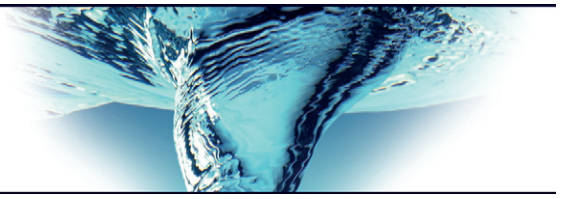

JFM RAPIDS
journals.cambridge.org/rapids

Acoustic receptivity simulations of flow past a flat plate with elliptic leading edge

Nima Shahriari[1,†], Daniel J. Bodony[2], Ardeshir Hanifi[1,3] and Dan S. Henningson[1]

[1]Department of Mechanics, Linné FLOW Centre and Swedish e-Science Research Centre (SeRC), KTH Royal Institute of Technology, SE-100 44 Stockholm, Sweden

[2]Department of Aerospace Engineering, University of Illinois at Urbana-Champaign, Illinois 61801, USA

[3]Swedish Defence Research Agency, FOI, SE-164 90 Stockholm, Sweden

(Received 6 April 2016; revised 17 May 2016; accepted 17 June 2016; first published online 13 July 2016)

We present results of numerical simulations of leading-edge acoustic receptivity for acoustic waves impinging on the leading edge of a finite-thickness flat plate. We use both compressible and incompressible flow solvers fitted with high-order high-accuracy numerical methods and independent methods of estimating the receptivity coefficient. The results show that the level of acoustic receptivity in the existing literature appears to be one order of magnitude too high. Our review of previous numerical simulations and experiments clearly identifies some contradictory trends. In the limit of an infinitely thin flat plate, our results are consistent with asymptotic theory and numerical simulations.

Key words: boundary layers, boundary layer receptivity, boundary layer stability

1. Introduction

An understanding of the laminar–turbulent transition process is crucial for design and optimisation in numerous aerodynamic applications. The practical and fundamental importance of the transition process has attracted extensive studies over several decades; however, all stages of the transition process are not yet fully understood. A critical one is the so-called receptivity stage, through which the external perturbations trigger instability waves. Transition often occurs when the amplitude of the instability waves reaches a certain critical level. Therefore, for a given flow, the location of transition strongly depends on the initial amplitude of the perturbations, making an understanding of the receptivity mechanisms a critical part of transition prediction capability.

† Email address for correspondence: nima@mech.kth.se

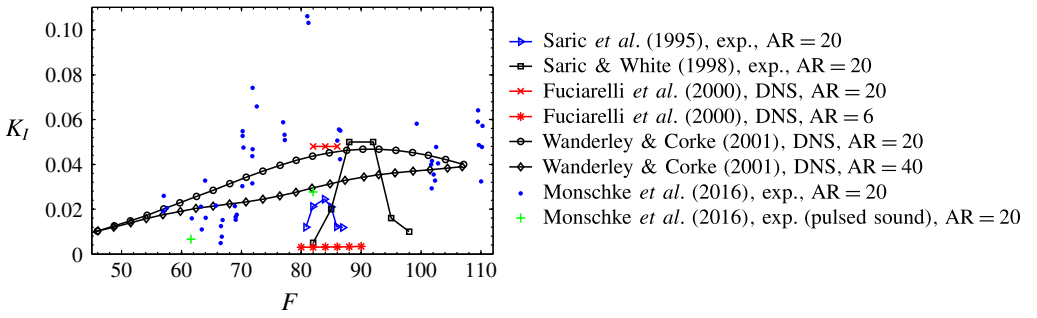

FIGURE 1. Branch I acoustic receptivity coefficient of the current major numerical and experimental works on the MSE leading-edge geometry with different aspect ratios.

In the present work, we investigate the response of the boundary layer on a finite-thickness flat plate with an elliptic leading edge to acoustic plane waves. Acoustic disturbances that enter the boundary layer excite a variety of unsteady modes, including the Stokes and Tollmien–Schlichting (TS) waves. Measurement of the amplitude of the TS waves created by the acoustic field is a challenging task due to the presence of Stokes waves with the same temporal frequency as the TS waves. This problem has earlier been studied both experimentally (Saric & White 1998; Monschke, Kuester & White 2016) and numerically (Fuciarelli, Reed & Lyttle 2000; Wanderley & Corke 2001). However, the published results present a scattered picture of the receptivity coefficients. In some cases these results show contradictory trends with respect to variations of the leading-edge geometry.

We focus on the flow case of a flat plate with modified super-elliptic (MSE) leading edge. The MSE leading edge has zero curvature at the junction with the flat plate to minimise the undesired localised receptivity due to geometric discontinuities (Goldstein & Hultgren 1989). Figure 1 summarises the acoustic receptivity coefficients of the existing major studies on the MSE geometry with different aspect ratios (ARs) but constant plate half-thickness Reynolds number of $Re_b = 2400$ and Mach numbers less than 0.1. Here, one can observe considerable scatter in the reported receptivity coefficients, i.e. an order of magnitude, in some frequency ranges. It can be noted from figure 1 that there exists a large amount of scatter in the experimental data, both within each experiment and between different sets.

Another important observation is the discrepancy in the trends seen in the direct numerical simulation (DNS) data of Fuciarelli *et al.* (2000) and Wanderley & Corke (2001) to changes in AR. The results of the latter simulations show a decrease of receptivity coefficient with increasing MSE aspect ratio. This trend is in agreement with that reported in the numerical work by Lin, Reed & Saric (1992) and experimental work by Wlezien (1994). However, the computed data by Fuciarelli *et al.* (2000) show the opposite trend. These data show a reduction of the receptivity coefficient by an order of magnitude when the leading-edge ratio is reduced from 20 to 6. The wide spread of the data shown in figure 1 demonstrates that the existing perception of the acoustic receptivity coefficient for geometries with MSE leading edge is ambiguous and inconclusive.

The objective of this work is to revisit this problem and perform DNS in order to resolve the abovementioned ambiguities. The simulations are performed using compressible and incompressible models of the same flow, using different high-order

methods for cross-verification. Accurate extraction of the TS wave amplitude is ensured by using methods proposed by Murdock (1980) and Wlezien (1994).

2. Flow configuration and numerical approach

2.1. Geometry and flow parameters

The flow around a semi-infinite flat plate with an MSE leading edge is considered for investigation. This geometry follows the suggestion by Lin *et al.* (1992) and is defined as

$$\left(\frac{y}{b}\right)^2 + \left(\frac{a-x}{a}\right)^m = 1, \quad \text{with } m = 2 + \left(\frac{x}{a}\right)^2, \tag{2.1}$$

where x and y are the streamwise and wall-normal coordinates respectively. The parameters a and b are the semi-major and semi-minor axes of the ellipse. The aspect ratio of the ellipse is defined as $\mathrm{AR} \equiv a/b$, measuring the curvature of the leading edge.

The semi-minor axis of the ellipse, b, is chosen as the reference length scale in this study. The reference velocity at the inflow, U_∞, and the kinematic viscosity, ν, are chosen in such a way that the Reynolds number becomes $Re_b = U_\infty b/\nu = 2400$. The length of the computational domain in the downstream direction is $L = 450$ units (in terms of the plate half-thickness), which corresponds to a Reynolds number of $Re_L = U_\infty L/\nu = 1.08 \times 10^6$ at the end of the domain. This length is sufficient to accommodate the second branch of the neutral stability curve for the considered frequencies in this study. The extent of the domain in the wall-normal direction and upstream of the leading edge is 400 units, which is 200 times larger than the maximum boundary layer thickness in the considered domain.

2.2. Direct numerical simulations

We use two different flow models. Considering first an incompressible model, the incompressible Navier–Stokes equations are integrated in time using the `NEK5000` code developed by Fischer, Lottes & Kerkemeier (2008). `NEK5000` is based on the spectral element method (SEM) to provide geometrical flexibility, spectral accuracy and efficient parallelisation. The physical domain in the SEM is decomposed into spectral elements where the local approximation of the flow field is obtained as a sum of Lagrange interpolants defined by an orthogonal basis of Legendre polynomials up to degree N. In the main part of this study we have used $N = 8$. The time integration is a third-order scheme.

For the baseflow computation using the incompressible fluid solver, no-slip and no-penetration boundary conditions are imposed on the solid surface. The far-field boundary conditions are of Dirichlet type, obtained from a potential-flow solution around a corresponding body thickened by the displacement thickness of the evolving boundary layer. Along the stagnation streamline, a symmetric boundary condition has been employed to reduce the computational cost. The outflow boundary condition is the natural condition derived from the weak form of the Navier–Stokes equations. More detail on this topic can be found in Schrader *et al.* (2010).

Our second flow model does not assume incompressibility and solves the compressible Navier–Stokes equations in curvilinear coordinates using high-order finite differences. A globally fifth-order explicit summation-by-parts scheme (Strand 1994) is used for spatial discretisation that is fourth-order accurate on the boundary and eighth-order accurate in the interior. The divergence of the viscous fluxes is

Simulation	AR	$N_x \times N_y$	ΔS_{min}	ΔS_{max}	Δy_{min}
Incompressible	6	587×128	3.391×10^{-2}	2.3817	0.02
Incompressible	20	554×128	3.304×10^{-2}	2.3817	0.02
Incompressible	40	526×128	1.718×10^{-2}	2.3817	0.02
Compressible	20	809×257	6.185×10^{-4}	0.7692	0.002

TABLE 1. The parameters of the computational grids: N_x and N_y denote the numbers of elements/grid points in the streamwise and wall-normal directions; ΔS_{min} and ΔS_{max} are the minimum and maximum element sizes/grid spacings along the surface; Δy_{min} is the minimum element size/grid spacing normal to the surface.

computed using analytical second derivative operators, which add, in the domain interior, dissipation at the highest wavenumber. No artificial dissipation is used. The equations are advanced in time using an explicit fourth-order Runge–Kutta method.

Simultaneous-approximation-term (SAT) boundary conditions are used on all boundaries except the outflow to enforce isothermal no-slip conditions on the wall (Svärd & Nordström 2008) and the far-field (Svärd, Carpenter & Nordström 2007) conditions. Non-reflecting boundary conditions are used at the outflow. These boundary conditions are numerically stable and have been shown by Bodony (2010) to be accurate in aeroacoustic problems. Sponge regions are located adjacent to the far-field and outflow boundaries in the baseflow computation to dampen unwanted acoustic reflections as well as to impose the incident acoustic waves (Bodony 2006).

The compressible equations are non-dimensionalised with respect to the ambient reference variables, density ρ_∞, speed of sound a_∞, viscosity μ_∞ and the plate half-thickness b as the reference length scale. The free-stream velocity and the plate half-thickness are chosen to have $Re_b = U_\infty b/\nu = 2400$. We set the Mach number at 0.1.

The computational mesh is designed such that elements/grid points are clustered towards the wall and the leading edge, using geometric stretching, to resolve the boundary layer. The mesh is designed to have a minimum of 20 grid points per instability wavelength (predicted by the local theory) in the streamwise direction. Table 1 summarises the parameters of the different grids used in this study.

2.3. *Perturbed flow*

Acoustic wave disturbances within an incompressible framework are modelled by superposing a periodic fluctuation in the form of $u' = \varepsilon \cos(\omega t)$, with angular frequency $\omega/2\pi$ and amplitude ε, on the streamwise velocity component of the far-field boundary similarly to Fuciarelli *et al.* (2000) and Wanderley & Corke (2001). Therefore, the far-field boundary condition would be to enforce $u = U_\infty(1 + \varepsilon \cos(\omega t))$. The 'acoustic' waves of such form have zero spatial wavenumber, resulting in an infinite-wavelength acoustic wave model. We set the acoustic perturbation amplitude to $\varepsilon = 10^{-3}$ to generate a uniform oscillation with a maximum amplitude of $0.1\,\%U_\infty$.

In the compressible simulations, planar acoustic waves are generated through the far-field boundary condition and are enforced by the sponge zone similarly to the work by Zhang & Bodony (2012). These waves are imposed at the far-field boundary as well as in the sponge zone, and propagate to the leading edge by the nonlinear equations of motion. The amplitude of the acoustic waves corresponds to 101 dB, as used by Saric & White (1998). The length of the sponge zone in the far field can accommodate a minimum of one acoustic wavelength of the smallest frequency considered.

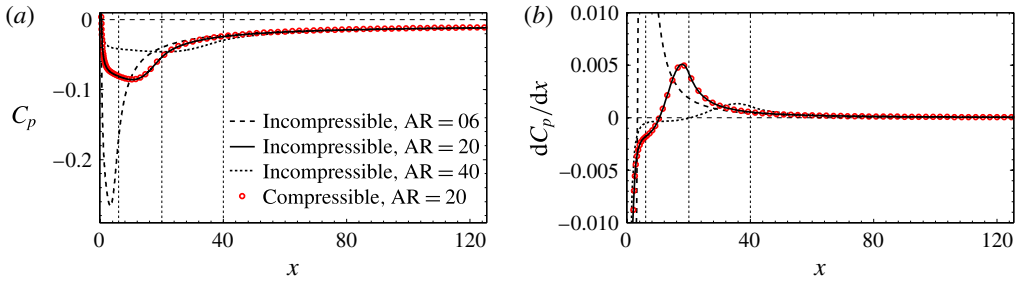

FIGURE 2. (*a*) Pressure coefficient distribution C_p and (*b*) its chordwise derivative as a function of the streamwise coordinate. The vertical dashed lines depict the junction of the leading edge and the flat plate.

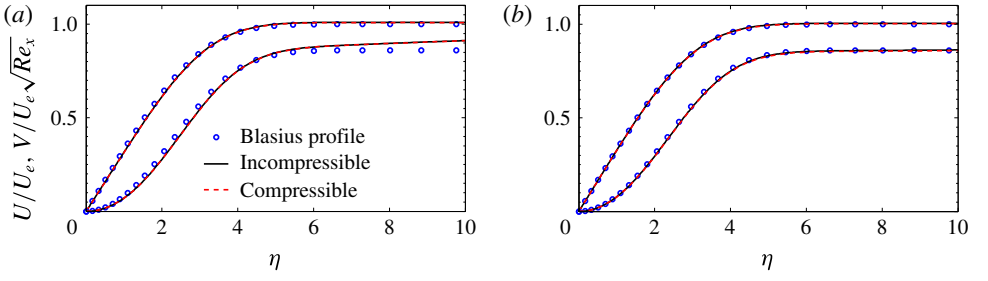

FIGURE 3. Comparison of the streamwise and wall-normal velocity profiles with the Blasius similarity solution, (*a*) at the streamwise location $x = 50$, $Re_x = 1.2 \times 10^5$ and (*b*) at the streamwise location $x = 200$, $Re_x = 4.8 \times 10^5$; 20 : 1 MSE leading edge.

3. Results

3.1. *Basic state*

A steady-state solution resolved in space and converged in time is calculated prior to performing the simulations with the incident perturbations. The baseflow is used in the perturbation simulations as the target state in the sponge regions. In addition, computation of the baseflow enables us to cross-check the results between the codes. The governing equations are integrated in time until a steady-state baseflow is reached. We consider the baseflow to be converged in time when the time derivative of the flow variables is below $O(10^{-11})$.

Figures 2(*a*) and 2(*b*) show the distribution of the surface pressure coefficient C_p and its chordwise derivative as functions of the streamwise coordinate. As is seen in these figures, there is a local region of favourable pressure gradient near the leading edge where the flow accelerates followed by a region of adverse pressure gradient where the flow decelerates moving downstream. Sufficiently far downstream of the leading edge, the pressure gradient is small and the flow can be considered to be of Blasius type. A comparison between the Blasius similarity solution and the velocity profiles obtained by DNS is shown in figure 3 for streamwise positions of $x = 50$ and 200. At the former location, a deviation from the Blasius profile is apparent due to the presence of the pressure gradient. At the latter location both velocity components closely match the Blasius profile.

There is a good match between the compressible and incompressible results, as shown in figures 2 and 3 for the baseflow computation. This close match demonstrates the correctness of the numerical set-up in both codes and the sufficient resolution for baseflow computation. A resolution study (p-refinement) was performed for the incompressible simulation, where the results obtained using polynomial orders of 8 and 10 are on top of each other. Grid convergence of the compressible baseflow was also demonstrated in this study (not shown).

3.2. *Perturbed flow and TS wave extraction*

A number of simulations with small-amplitude acoustic perturbations and different dimensionless frequencies were performed. As a result, the perturbed flow is harmonic in time with the prescribed acoustic frequency. A fast Fourier transform in time is applied on the flow-field snapshots to obtain the Fourier amplitude of the perturbations.

In order to extract the TS wave amplitude from the total perturbation amplitude, we follow the method proposed by Murdock (1980). He suggests that the magnitude of the spatial mean of the disturbances is associated with the sound wave and the magnitude of the envelope about the mean is associated with the TS wave. For our incompressible flow model, the solution inside the boundary layer is composed of a Stokes wave with infinite wavelength ($\alpha_{Stokes} = 0$) and a TS wave with a finite wavelength:

$$u = \mathrm{Re}\{A_{Stokes}\, \mathrm{e}^{-\mathrm{i}\omega t} + A_{TS}\, \mathrm{e}^{-\mathrm{i}\omega t + \mathrm{i}\alpha_{TS} x}\}. \tag{3.1}$$

We have assumed that the Stokes and TS amplitudes are independent or weakly dependent and that they are functions of the wall-normal direction and slowly varying functions of the streamwise coordinate. The complex Fourier amplitude of the solution at the frequency ω is $\hat{u} = A_{Stokes} + A_{TS}\, \mathrm{e}^{\mathrm{i}\alpha_{TS} x}$, and the magnitude of the amplitude reads as

$$|\hat{u}| = (A_{Stokes}^2 + A_{TS}^2 + 2A_{Stokes} A_{TS} \cos(\alpha_{TS} x))^{1/2}. \tag{3.2}$$

If the TS wave amplitude is much smaller than the Stokes wave amplitude, $A_{Stokes} \gg A_{TS}$, relation (3.2) can be expanded using a Taylor series, which results in

$$|\hat{u}| = A_{Stokes} + A_{TS} \cos(\alpha_{TS} x) + O(A_{TS}^2). \tag{3.3}$$

Equation (3.3) shows that the Fourier amplitude of the total disturbance oscillates spatially around a mean value A_{Stokes}, with the amplitude and wavelength of the TS wave.

Figure 4(a) shows the evolution of the total streamwise velocity fluctuations at a constant distance of 0.2 from the wall, demonstrating that the perturbations oscillate spatially with the TS wavelength. Furthermore, it is apparent that the amplitude of the Stokes wave is affected by the strong pressure gradients present up to the lower-branch region. Therefore, without loss of the generality in the decomposition method, we only consider streamwise locations downstream of the lower branch where the Stokes layer has a nearly constant thickness. The TS wave amplitude is extracted at the upper-branch location and scaled down to the lower branch using the amplitude ratio computed by the parabolised stability equations (PSE). Figure 5(a) shows the distribution of the maximum streamwise perturbation velocity normalised by the free-stream disturbance amplitude for the incompressible data. Following the extraction method by subtracting the mean of the signal, illustrated with the red line,

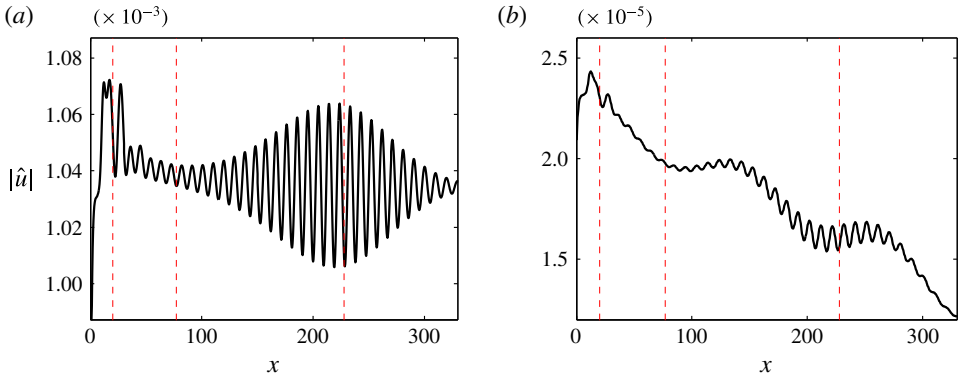

FIGURE 4. The streamwise perturbation amplitude distribution in the streamwise direction at a constant distance of 0.2 from the surface: (*a*) the incompressible and (*b*) the compressible results. The vertical dashed lines from left to right indicate the junction with the flat plate, and the lower and upper branches of the neutral curve respectively; 20 : 1 MSE leading edge with dimensionless frequency of $F = 100$.

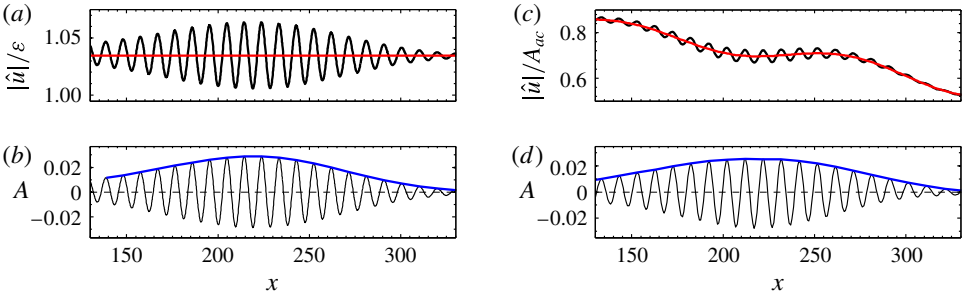

FIGURE 5. The distribution of the maximum streamwise perturbation amplitude, normalised by the amplitude of the acoustic wave at free stream in (*a*) the incompressible and (*c*) the compressible simulation. The red lines illustrate the global and local means of the signal shown respectively. Plots of (*b*) $A = |\hat{u}|/\varepsilon - \text{mean}(|\hat{u}|/\varepsilon)$ and (*d*) $A = |\hat{u}|/A_{ac} - \text{mean}(|\hat{u}|/A_{ac})$, showing the streamwise evolution of the TS wave amplitude in blue; 20 : 1 MSE leading edge and $F = 100$.

the envelope of the remainder is the TS wave amplitude shown with the blue line in figure 5(*b*). A resolution study using polynomial orders of 8 and 10 has confirmed these results.

The same analogy is valid for extracting the TS wave amplitude from the compressible data. As shown in figure 4(*b*), the acoustic wave in the compressible simulations has a long finite wavelength, contrary to the infinite wavelength in the incompressible framework. Therefore, in order to remove the acoustic wave from the total compressible perturbation signal, a local average of the total signal is used in contrast to the global average (mean) in the incompressible case. The local average is calculated by taking the convolution of the signal with a spatial Gaussian window, with a window length that is three times the TS wavelength. Figure 5(*c*) shows the maximum amplitude of the total perturbations normalised by the amplitude of the free-stream acoustic wave, A_{ac}, in black and the local average of the signal

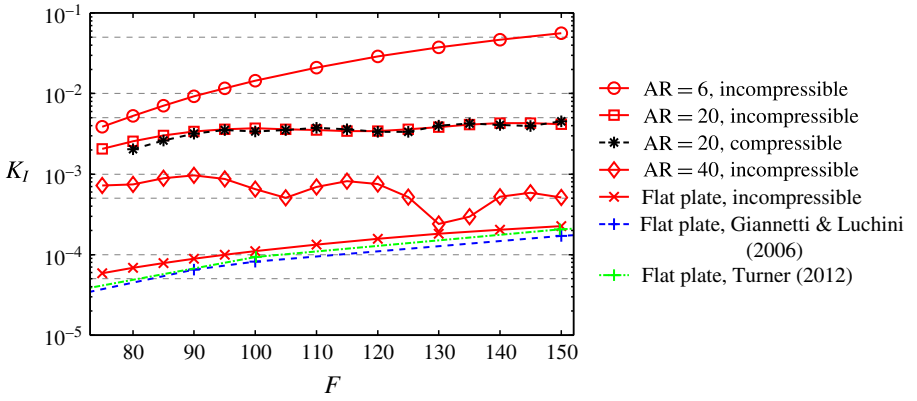

FIGURE 6. The branch I acoustic receptivity coefficient as a function of the reduced frequency.

in red. Subtraction of the total amplitude from the local averaged one is shown in figure 5(*d*), where the envelope of the remaining signal is the TS wave amplitude. The independence of the results with regard to the local averaging window size has been ensured by varying the window length. Grid refinement studies have confirmed these results.

3.3. *Receptivity coefficient*

The branch I receptivity coefficient, K_I, is defined as the ratio of the TS wave amplitude and the acoustic wave amplitude,

$$K_I = \frac{|\hat{u}_{TS}|_I}{u_{ac}} = \frac{|\hat{u}_{TS}|_{II}}{e^N u_{ac}}, \tag{3.4}$$

where N is the integrated growth rate from branch I to branch II. This definition of the receptivity coefficient includes the effects of both the leading edge and the subsequent pressure distribution at the branch I location. The amplitude of the acoustic wave, u_{ac}, is measured in the free stream. Here, it is equal to $\varepsilon = 10^{-3}$ in the incompressible simulations and $A_{ac} = 2.13 \times 10^{-5}$ (equivalent to 101 dB) in the compressible simulations.

Figure 6 shows the branch I acoustic receptivity coefficient as a function of the dimensionless frequency for three different MSE leading-edge ARs and the infinitely thin flat-plate geometry. There is an excellent agreement between the results of the incompressible and compressible simulations, validating the numerical set-up for each code, the TS wave extraction procedure and, therefore, the results.

It is evident from figure 6 that the receptivity coefficient increases by reducing the leading-edge aspect ratio. In other words, leading-edge bluntness enhances the branch I acoustic receptivity. This is due to the fact that a blunter leading edge has a larger (in magnitude) local adverse pressure gradient in the leading-edge region (see figure 2), which has a destabilising effect on the evolution of TS waves. This trend is in agreement with the previous numerical work by Lin *et al.* (1992) and the experiment of Wlezien (1994). Moreover, Lin *et al.* (1992) report that the receptivity coefficient for AR = 6 is of order 10^{-1} at a frequency of $F = 2\pi f\nu/U_\infty^2 \times 10^6 = 230$, which is in good agreement with our result, $K_I = 0.12$ for the same frequency (not shown in figure 6).

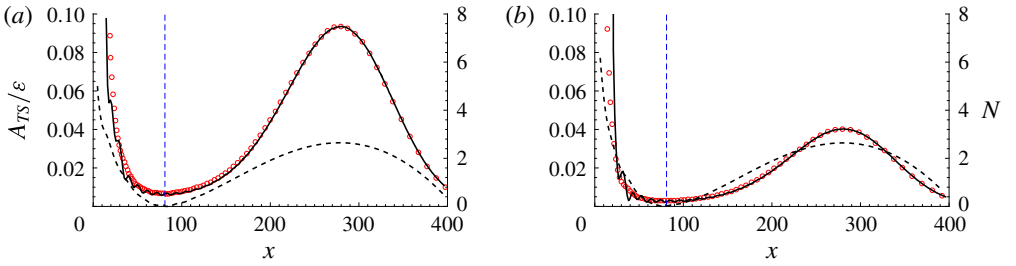

FIGURE 7. The distribution of (——) the TS wave amplitude, extracted using the method proposed by Wlezien (1994), (– – – –) the N-factor and (○) the TS wave amplitude extrapolated from the branch II location using PSE: (*a*) 6 : 1 MSE and (*b*) 20 : 1 MSE; $F = 85$.

In the limit of an infinitely thin flat plate, the receptivity coefficient is in close agreement with the asymptotic results of Giannetti & Luchini (2006) and the PSE results of Turner (2012). The numerical set-up for this case includes the leading edge of the flat plate and the upstream region. Moreover, we observe close agreement with the DNS result of Murdock (1980), where he reports $K_I = 5.5 \pm 1.5 \times 10^{-5}$ for $F = 56$. The agreement between our results for an infinitely thin flat plate and other works based on the asymptotic theory, PSE and DNS serves as another validation of the presented results.

Fuciarelli *et al.* (2000) use the decomposition method proposed by Wlezien (1994) to extract the TS wave amplitude. For the sake of comparison, we have used the same procedure to obtain the TS wave amplitude in our simulations for the incompressible flow. The results are presented in figure 7 for $F = 85$, AR $= 6$ and 20. Here also the extrapolated amplitude from branch II using PSE is shown. As can be seen, there is a good match between the extracted TS wave amplitude and the extrapolated one. The TS wave amplitudes at the branch II location obtained by Wlezien (1994) and the method of Murdock (1980) are practically the same, which results in the identical branch I receptivity coefficients presented in figure 6.

4. Discussion and conclusions

The acoustic receptivity coefficients presented in figure 6 for the MSE geometries are approximately one order of magnitude smaller than the values in the existing results shown in figure 1. In order to understand the reasons for this mismatch, we attempt to point out inconsistencies that exist in the literature.

Employing asymptotic theory, Kerschen, Choudhari & Heinrich (1990) predicted that the leading-edge receptivity coefficient, K_{LE}, is of order of unity for planar acoustic waves propagating parallel to the wall surface. This coefficient can be used to estimate the order of magnitude of the branch I receptivity coefficient as $K_I = K_{LE}/\mathrm{e}^N$, where N is the integrated growth rate (N-factor) from the branch I location to the leading edge. The evolution of the N-factor in the streamwise direction is computed using PSE and shown in figure 7. At the reduced frequency of $F = 85$, the N-factors for the MSE leading edges with AR $= 6$ and 20 are $N = 5$ and $N = 6.2$ respectively. Assuming that the asymptotic leading-edge coefficient is $K_{LE} = 1$, the receptivity coefficient at branch I is expected to be $K_I = 1/\mathrm{e}^N = 0.0065$ for the 6 : 1 MSE leading edge and $K_I = 0.002$ for the 20 : 1 MSE leading edge, an approximate

magnitude of 10^{-3}. The results of the present study are within this range, while all of the existing results in the literature for the 20 : 1 MSE leading edge are one order of magnitude larger than the estimated value.

The reason for the discrepancies within the experimental data of Saric, Wei & Rasmussen (1995), Saric & White (1998) and Monschke *et al.* (2016), in which the same physical model and wind tunnel were used, is unclear. However, those experiments used three different measurement techniques and were conducted over a 20-year span. Moreover, these measurements are extremely difficult and sensitive to many factors. This makes it possible that even a small bias could have a significant impact on the experimental results, with one plausible reason being acoustically excited leading-edge vibration (private communication, W. S. Saric & E. B. White).

Regarding the computational studies, in the computational work of Fuciarelli *et al.* (2000) their domain does not include the branch I location for their frequency range. Therefore, they extrapolate the TS wave amplitude measured upstream of branch I to the first neutral point using local stability theory. The report by Fuciarelli *et al.* (2000) is concentrated on a leading edge with an aspect ratio of AR = 6. Their reported results for this geometry are in agreement with our simulations ($K_I = 0.0030$–0.0034 for $F = 80$–90). Their results for AR = 20, being one order of magnitude higher ($K_I = 0.04$), only appear in a table where the data are compared with the experimental values. Unfortunately, Fuciarelli *et al.* (2000) do not report the amplitude decay ratio for the AR = 20 case. Using the amplitude ratio from our PSE analysis, we find a leading-edge receptivity coefficient of order 10, which is one order of magnitude higher than the expected value based on the work of Kerschen *et al.* (1990). Moreover, in agreement with the DNS of Lin *et al.* (1992) and the experiment of Wlezien (1994), the branch I receptivity coefficient in the current study is found to be larger for blunter leading-edge shapes. Fuciarelli *et al.* (2000), however, report a larger receptivity coefficient (one order of magnitude) for the 20 : 1 MSE leading edge compared with the 6 : 1 MSE leading edge. This suggests that their reported values for AR = 20 are incorrectly tabulated.

The receptivity coefficient reported by Wanderley & Corke (2001) is obtained by considering the amplitude of the TS wave directly at the branch I location. However, Turner (2012) shows by replicating their TS wave extraction method that the amplitude of the TS wave in the lower-branch region is contaminated by the remnants of the Stokes layer, not removed by their filtering process. Indeed, by extrapolating the upper-branch TS amplitudes reported in Wanderley (1998) to the lower branch, the receptivity coefficient K_I is found to be at least half of the values reported in Wanderley & Corke (2001). Furthermore, in the latter study, which is based on a second-order-accurate numerical method, only 36 grid points have been used to resolve the whole domain in the wall-normal direction. In contrast, the numerical resolution in the present study is at least five times that of Wanderley & Corke (2001). Using the parameters they give, we were unable to obtain a numerically converged solution using the `NEK5000` which has spectral accuracy.

Using cross-verified simulations with different flow models and identifying numerical explanations for large-K_I predictions from previous simulations, we thus conclude that the current receptivity predictions are accurate and one order of magnitude smaller than the existing values in the literature.

Acknowledgements

The authors would like to acknowledge Professors W. Saric, H. Reed and E. White for fruitful discussions. Their interest has been very much appreciated. This work has

been supported by the European commission through Clean Sky project RODTRAC (grant agreement no. CS-GA-2011-01-296507). Computer time provided by SNIC (Swedish National Infrastructure for Computing) is gratefully acknowledged.

References

BODONY, D. J. 2006 Analysis of sponge zones for computational fluid mechanics. *J. Comput. Phys.* **212** (2), 681–702.

BODONY, D. J. 2010 Accuracy of the simultaneous-approximation-term boundary condition for time-dependent problems. *J. Sci. Comput.* **43** (1), 118–133.

FISCHER, P. F., LOTTES, J. W. & KERKEMEIER, S. G. 2008 NEK5000 Web page. http://nek5000.mcs.anl.gov.

FUCIARELLI, D., REED, H. & LYTTLE, I. 2000 Direct numerical simulation of leading-edge receptivity to sound. *AIAA J.* **38** (7), 1159–1165.

GIANNETTI, F. & LUCHINI, P. 2006 Leading-edge receptivity by adjoint methods. *J. Fluid Mech.* **547**, 21–53.

GOLDSTEIN, M. E. & HULTGREN, L. S. 1989 Boundary-layer receptivity to long-wave free-stream disturbances. *Annu. Rev. Fluid Mech.* **21** (1), 137–166.

KERSCHEN, E. J., CHOUDHARI, M. & HEINRICH, R. A. 1990 Generation of boundary layer instability waves by acoustic and vortical free-stream disturbances. In *Laminar-Turbulent Transition*, pp. 477–488. Springer.

LIN, N., REED, H. & SARIC, W. S. 1992 Effect of leading-edge geometry on boundary-layer receptivity to freestream sound. In *Instability, Transition, and Turbulence*, pp. 421–440. Springer.

MONSCHKE, J. A., KUESTER, M. S. & WHITE, E. B. 2016 Acoustic receptivity measurements using modal decomposition of a modified Orr–Sommerfeld equation. *AIAA J.* **54** (3), 805–815.

MURDOCK, J. W. 1980 The generation of a Tollmien–Schlichting wave by a sound wave. *Proc. R. Soc. Lond.* A **372** (1751), 517–534.

SARIC, W. S., WEI, W. & RASMUSSEN, B. K. 1995 Effect of leading edge on sound receptivity. In *Laminar–Turbulent Transition*, pp. 413–420. Springer.

SARIC, W. S. & WHITE, E. B. 1998 Influence of high-amplitude noise on boundary-layer transition to turbulence. *AIAA Paper* 98-2645.

SCHRADER, L. U., BRANDT, L., MAVRIPLIS, C. & HENNINGSON, D. S. 2010 Receptivity to free-stream vorticity of flow past a flat plate with elliptic leading edge. *J. Fluid Mech.* **653**, 245–271.

STRAND, B. 1994 Summation by parts for finite difference approximations for d/dx. *J. Comput. Phys.* **110** (1), 47–67.

SVÄRD, M., CARPENTER, M. H. & NORDSTRÖM, J. 2007 A stable high-order finite difference scheme for the compressible Navier–Stokes equations, far-field boundary conditions. *J. Comput. Phys.* **225** (1), 1020–1038.

SVÄRD, M. & NORDSTRÖM, J. 2008 A stable high-order finite difference scheme for the compressible Navier–Stokes equations: no-slip wall boundary conditions. *J. Comput. Phys.* **227** (10), 4805–4824.

TURNER, M. R. 2012 Tollmien–Schlichting wave amplitudes on a semi-infinite flat plate and a parabolic body: comparison of a parabolized stability equation method and direct numerical simulations. *Q. J. Mech. Appl. Maths* **65** (2), 183–210.

WANDERLEY, J. B. V. 1998 Numerical simulation of receptivity to acoustic waves on elliptic leading edges. PhD thesis, Illinois Institute of Technology.

WANDERLEY, J. B. V. & CORKE, T. C. 2001 Boundary layer receptivity to free-stream sound on elliptic leading edges of flat plates. *J. Fluid Mech.* **429**, 1–21.

WLEZIEN, R. 1994 Measurement of acoustic receptivity. *AIAA Paper* 94-2221.

ZHANG, Q. & BODONY, D. J. 2012 Numerical investigation and modelling of acoustically excited flow through a circular orifice backed by a hexagonal cavity. *J. Fluid Mech.* **693**, 367–401.